

# New classes of quantum anomalous Hall crystals in multilayer graphene

Boran Zhou<sup>1</sup> and Ya-Hui Zhang<sup>1</sup>

<sup>1</sup>*Department of Physics and Astronomy, Johns Hopkins University, Baltimore, Maryland 21218, USA*  
(Dated: November 8, 2024)

The recent experimental observation of quantum anomalous Hall (QAH) effects in the rhombohedrally stacked pentalayer graphene has motivated theoretical discussions on the possibility of quantum anomalous Hall crystal (QAHC), a topological version of Wigner crystal. Conventionally Wigner crystal was assumed to have a period  $a_{\text{crystal}} = 1/\sqrt{n}$  locked to the density  $n$ . In this work we propose new types of topological Wigner crystals labeled as QAHC- $z$  with period  $a_{\text{crystal}} = \sqrt{z/n}$ . In rhombohedrally stacked graphene aligned with hexagon boron nitride (hBN), we find parameter regimes where QAHC-2 and QAHC-3 have lower energy than the conventional QAHC-1 at total filling  $\nu = 1$  per moiré unit cell. These states all have total Chern number  $C_{\text{tot}} = 1$  and are consistent with the QAH effect observed in the experiments. The larger period QAHC states have better kinetic energy due to the unique Mexican-hat dispersion of the pentalayer graphene, which can compensate for the loss in the interaction energy. Unlike QAHC-1, QAHC-2 and QAHC-3 also break the moiré translation symmetry and are sharply distinct from a moiré band insulator. We also briefly discuss the competition between integer QAH and fractional QAH states at filling  $\nu = 2/3$ . Besides, we notice the importance of the moiré potential. A larger moiré potential can greatly change the phase diagram and even favors a QAHC-1 ansatz with  $C = 2$  Chern band.

**Introduction** Fractional quantum anomalous Hall (FQAH) effects, defined as fractional quantum Hall (FQH) effects [1, 2] at zero magnetic field, have been theoretically proposed to be possible in a narrow Chern band [3–11]. In recent years, various moiré systems have been proposed as promising candidates [12–22]. Integer quantum anomalous Hall (QAH) effects have been reported in twisted bilayer graphene (TBG) aligned with hexagon boron nitride (hBN) [23, 24], ABC-trilayer graphene/hBN moiré system [25], transition metal dichalcogenide (TMD) moiré heterobilayers [26] and homobilayers [27]. Later, FQAH was finally realized in twisted MoTe<sub>2</sub> homobilayers [28–31] and rhombohedrally stacked pentalayer graphene [32, 33]. In twisted MoTe<sub>2</sub>, the first valence band has a nonzero Chern number  $C = 1$  [13, 34, 35], resembling a Landau level, which makes FQAH states at fractional fillings quite natural. In contrast, in the pentalayer graphene system, even the integer QAH effect at  $\nu = 1$  is a surprise because the moiré potential is too weak to open a band gap.

Theoretical progress has been made to understand the integer filling  $\nu = 1$  for pentalayer graphene [36–44]. Although there is no band gap at the single particle level because electrons are pushed to layers far away from the aligned hBN and feel only a weak moiré potential, Hartree Fock calculations [36–38, 40, 41] show that interactions can spontaneously generate a large crystal potential at the mean field level, providing a narrow Chern band with  $C = 1$ . In the limit of a vanishing moiré potential, the phase is a topological version of Wigner crystal, dubbed as quantum anomalous Hall crystal (QAHC) [37, 38]. Similar physics is predicted to appear in rhombohedrally stacked  $n_{\text{layer}}$ -layer graphene with  $n_{\text{layer}} = 4, 6, 7$ , later verified by experiments [45–48]. The new concept of QAHC has attracted lots of attentions [49–54]. However, there are debates on whether the QAH insulator is really different from a moiré band

insulator and the role of the moiré potential [55]. In this paper we ask the following question: can we find a QAHC state which also breaks the moiré translation symmetry, thereby sharply distinguished from a moiré band insulator? If an integer QAH effect is realized at fractional filling, it is guaranteed to break translation symmetry, as observed in twisted bilayer-trilayer graphene [56]. Here we present surprising results showing that even the integer QAH insulator at  $\nu = 1$  may break moiré translation symmetry.

Given that the moiré potential is a perturbation, we can first consider the moiréless limit. We extend the quantum anomalous Hall crystal concept and use QAHC- $z$  to label a crystal with a unit cell size  $z$  times larger than the usual QAHC or Wigner crystal. Specifically, the crystal period is given by  $a_{\text{crystal}} = \sqrt{z/n}$ , where  $n$  is the electron density. Previous Hartree Fock calculations were restricted to QAHC-1 without any enlargement of the unit cell at  $\nu = 1$ . In contrast, we also include the possibilities of QAHC-2 and QAHC-3 in our new Hartree Fock calculations and find that they can be favored in certain parameter space spanned by the twist angle and the displacement field  $\delta_D$ . These new crystals have 2 or 3 bands fully occupied, but still have a total Chern number  $C_{\text{tot}} = 1$ , consistent with the QAH effect with  $\sigma_{xy} = e^2/h$ . Unlike QAHC-1, they break the moiré translation symmetry and are unambiguously beyond band insulator descriptions.

We also study the competition between integer QAHCs and FQAH states at fractional filling  $\nu = 2/3$ . Following the spirit of the variational method, we compare the energy of an FQAH state obtained by exact diagonalization (ED) and QAHCs from Hartree Fock calculations. We find that the FQAH state is usually at a lower energy and is increasingly favored with stronger interaction strengths and a stronger moiré potential. Among the integer QAH states, the QAHC-1 and QAHC-2 are in close

competitions, with either one being potentially favored depending on parameters. Hence we expect a rich phase diagram in rhombohedral multilayer graphene systems.

**Model** We employ the continuum model to calculate the bare band structure, with the Hamiltonian for each valley and spin given by:

$$H_K = H_0 + V_M H_M, \quad (1)$$

where  $H_0$  represents the Hamiltonian of rhombohedral pentalayer graphene:

$$H_0 = \begin{pmatrix} H_1 & \Gamma & \tilde{\Gamma} & \mathbf{0}_{2 \times 2} & \mathbf{0}_{2 \times 2} \\ \Gamma^\dagger & H_2 & \Gamma & \tilde{\Gamma} & \mathbf{0}_{2 \times 2} \\ \tilde{\Gamma}^\dagger & \Gamma^\dagger & H_3 & \Gamma & \tilde{\Gamma} \\ \mathbf{0}_{2 \times 2} & \tilde{\Gamma}^\dagger & \Gamma^\dagger & H_4 & \Gamma \\ \mathbf{0}_{2 \times 2} & \mathbf{0}_{2 \times 2} & \tilde{\Gamma}^\dagger & \Gamma^\dagger & H_5 \end{pmatrix}, \quad (2)$$

with the block matrices defined as follows:

$$H_i = \begin{pmatrix} (\frac{i}{4} - \frac{1}{2})\delta_D + u_{A,i} & -\frac{\sqrt{3}}{2}\gamma_0(\tilde{k}_x - i\tilde{k}_y) \\ -\frac{\sqrt{3}}{2}\gamma_0(\tilde{k}_x + i\tilde{k}_y) & (\frac{i}{4} - \frac{1}{2})\delta_D + u_{B,i} \end{pmatrix}, \quad (3)$$

$$\Gamma = \begin{pmatrix} -\frac{\sqrt{3}}{2}\gamma_4(\tilde{k}_x - i\tilde{k}_y) & -\frac{\sqrt{3}}{2}\gamma_3(\tilde{k}_x + i\tilde{k}_y) \\ \gamma_1 & -\frac{\sqrt{3}}{2}\gamma_4(\tilde{k}_x - i\tilde{k}_y) \end{pmatrix}, \quad (4)$$

$$\tilde{\Gamma} = \begin{pmatrix} 0 & \frac{1}{2}\gamma_2 \\ 0 & 0 \end{pmatrix}. \quad (5)$$

The parameters used are  $(\gamma_0, \gamma_1, \gamma_2, \gamma_3, \gamma_4) = (-2600, 358, -8.3, 293, 144)$  meV. The potential difference between the top and the bottom graphene layers is denoted by  $\delta_D$ .  $u_{A,1} = u_{B,5} = 0$ ,  $u_{B,1} = u_{A,5} = 12.2$  meV,  $u_{A,i} = u_{B,i} = -16.4$  meV for other terms. We rotate the graphene as  $\tilde{k}_x + i\tilde{k}_y = e^{i\theta_3}(k_x + ik_y)$ , where  $\theta_3 = \arctan \frac{\theta}{\delta_a}$  with  $\theta$  representing the twist angle between the graphene and the hBN.  $\delta_a = \frac{a_{\text{hBN}} - a_G}{a_{\text{hBN}}} = 0.017$ , where  $a_{\text{hBN}}$  and  $a_G$  are the lattice constants of graphene and hBN respectively.

The moiré potential, representing the tunneling between the first graphene layer aligned with the hBN, is given by:

$$H_M(\mathbf{G}_j) = \begin{pmatrix} C_0 e^{i\phi_0} + C_z e^{i\phi_z} & C_{AB} e^{i(\frac{(3-j)\pi}{3} - \phi_{AB})} \\ C_{AB} e^{i(\frac{(1+j)\pi}{3} - \phi_{AB})} & C_0 e^{i\phi_0} - C_z e^{i\phi_z} \end{pmatrix}, \quad (6)$$

where the momentum difference given by  $\mathbf{G}_j = \frac{4\pi}{\sqrt{3}L_M}(\cos(\frac{j\pi}{3} - \frac{5\pi}{6}), \sin(\frac{j\pi}{3} - \frac{5\pi}{6}))^T$  for  $j = 1, 3, 5$ . For  $j = 2, 4, 6$ , the tunneling is obtained by taking the Hermitian conjugate. The parameters are determined from DFT calculations [57] as  $C_0 = -10.13$  meV,  $\phi_0 = 86.53^\circ$ ,  $C_z = -9.01$  meV,  $\phi_z = 8.43^\circ$ ,  $C_{AB} = 11.34$  meV,  $\phi_{AB} = 19.60^\circ$ . Here we introduce an artificial parameter  $V_M$  in Eq. 1. We project the moiré potential onto the conduction bands to compare the energies for different  $V_M$  values (see the Appendix).

The interaction is given by the Coulomb potential:

$$H_V = \frac{1}{2A} \sum_{l,l'} \sum_{\mathbf{q}} V_{ll'}(\mathbf{q}) : \rho_l(\mathbf{q}) \rho_{l'}(-\mathbf{q}) :, \quad (7)$$

in which  $A$  is the area of the system,  $\rho_l(\mathbf{q})$  is the density in the layer  $l$ .  $V_{ll'}(\mathbf{q}) = \frac{e^2 \tanh q\lambda}{2\epsilon_0 \epsilon q} e^{-q|l-l'|d_{\text{layer}}}$ ,  $\lambda = 30$  nm is the screening length and  $d_{\text{layer}} = 0.34$  nm is the distance between adjacent layers. In all of the calculations, we use  $\epsilon = 10$  unless specified.

**Integer QAHC at  $\nu = 1$**  For the integer QAHC insulator at  $\nu = 1$  observed in recent experiments [32, 33, 45], we focus on the conduction bands. Due to the large and negative displacement field  $\delta_D$ , the conduction electrons mainly stay in the bottom layer, away from the aligned hBN on the top. As a consequence, the moiré potential projected onto the conduction band is less than 0.05 meV [37]. The previous theories suggest that the insulator at  $\nu = 1$  is a QAHC state [36–38] that is pinned by this small moiré potential. However, previous studies have been limited to crystals whose period is the same as the moiré period. In principle, the topological crystal state can have different crystal periods. We generalize the notion of QAHC to QAHC- $z$ , where  $z \in \mathbb{Z}$ , and the crystal period is labeled as  $a_{\text{crystal}} = \sqrt{z/\nu} a_M$ . The corresponding reciprocal lattice vector is represented as  $\mathbf{G}_i^{(z)}$ . For values of  $z/\nu = m_1^2 + m_2^2 + m_1 m_2$ , where  $m_1, m_2 \in \mathbb{Z}$ , the moiré potential is commensurate with the crystal period, allowing it to pin the crystal. For other values of  $z$ , the ground state energy remains unaffected by the moiré potential when treated as a first order perturbation.

**Phase diagram of QAHC crystals** We assume fully spin and valley polarization [12, 58] and perform HF calculations at  $\nu = 1$  for different QAHC- $z$  ansatzes. For each QAHC- $z$ , the calculation is conducted in a smaller Brillouin zone (BZ) scaled by  $1/\sqrt{z}$  relative to the moiré Brillouin zone (MBZ), with  $z$  electrons per unit cell. We compare the energies of different crystals with  $z = 1, 2, 3$  and select the one with the lowest energy. The resulting phase diagram is shown in Fig. 1(a). The anomalous Hall conductivity is determined by the total Chern number  $C_{\text{tot}}$  for the fully filled bands, i.e., first  $z$  HF conduction bands for QAHC- $z$ .  $C_{\text{tot}}$  is 0 or 1 in the whole phase diagram, consistent with previous studies restricted to the  $z = 1$  ansatz [36–38]. However, we now find two additional phases at  $V_M = 1$ : QAHC-2 and QAHC-3 with also  $C_{\text{tot}} = 1$ . Moreover, we manually increase the moiré potential by setting  $V_M$  to be 2 and 5 in Fig. 1(b)(c) to study the effect of a larger moiré potential. We note that QAHC-1 is favored by larger  $V_M$  as expected. For  $V_M = 5$ , there is also a  $C_{\text{tot}} = 2$  QAHC-1 state in some region of  $(a_M, \delta_D)$ , indicating the possibility of realizing higher Chern number in the pentalayer rhombohedral graphene system by enhancing the moiré potential. We also include results for a different parameter with  $|\gamma_0| = 3100$  meV in the appendix. There we find QAHC-2 occupies an even larger region for  $V_M = 1$ . Also for  $V_M = 2$ , we can already find QAHC-1 with  $C = 2$ . Although it is still not clear which parameter is more realistic, we can conclude that the QAHC-2 phase is possible and the  $C = 2$  QAHC insulator can be potentially stabilized with sufficiently larger  $V_M$ .

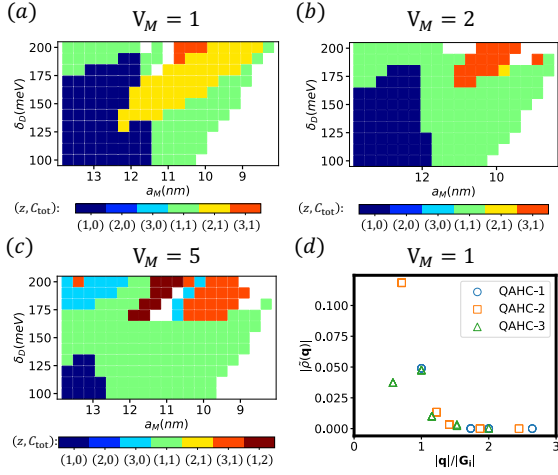


FIG. 1. HF calculation results at  $\epsilon = 10$ . (a) The phase diagram of QAHC as a function of displacement field  $D$  and moiré period  $a_M$  and  $V_M = 1$ . The label  $(z, C_{\text{tot}})$  represents the state is QAHC- $z$  with total Chern number  $C_{\text{tot}}$ . We keep  $N_{b,c}$  conduction bands and  $N_{b,v}$  valence bands in the calculation. For QAHC- $z$  with  $z = 1, 2, 3$ , we set  $N_{b,c}$  to 7, 7 and 9 respectively.  $N_{b,v}$  is taken as 0 for all values of  $z$ , since the valence bands are separated by the large displacement field. The calculations are performed using an  $N_k \times N_k$  grid in the crystal BZ. For  $z = 1, 2, 3$ , we set  $N_k$  to 12, 12 and 9 respectively. (b)(c) Similar to (a), but with  $V_M = 2, 5$  instead. (d) For  $\theta = 0.89^\circ$  ( $a_M = 10.7$  nm) and  $V_M = 1$ , displays of the function  $|\tilde{\rho}(\mathbf{q})|$  of QAHC-1 ( $\delta_D = 120$  meV), QAHC-2 ( $\delta_D = 160$  meV) and QAHC-3 ( $\delta_D = 210$  meV) respectively.

To distinguish different QAHC- $z$  states, one can measure the density distributions of conduction electrons, which is calculated as follows:

$$\rho(\mathbf{r}) = \sum_{\mathbf{q}} \tilde{\rho}(\mathbf{q}) e^{-i\mathbf{q}\cdot\mathbf{r}}, \quad (8)$$

$$\tilde{\rho}(\mathbf{q}) = \frac{1}{nN_k^2} \sum_{m_1, m_2, \mathbf{k}} \langle u_{\text{HF}, m_1}(\mathbf{k} + \mathbf{q}) | u_{\text{HF}, m_2}(\mathbf{k}) \rangle, \quad (9)$$

where  $k$  is defined in the crystal BZ, which is discretized into  $N_k \times N_k$  points. Here,  $|u_{\text{HF}, m_1}(\mathbf{k})\rangle$  represents the periodic part of the  $m_1^{\text{th}}$  conduction HF Bloch wavefunction, and  $m_1, m_2$  range over the values  $0, 1, \dots, N_{b,c} - 1$ .  $\mathbf{q} = n_1 \mathbf{G}_1 + n_2 \mathbf{G}_2$  corresponds to any integer linear combination of the crystal reciprocal lattice vectors. In Fig. 1(d), we compare  $\tilde{\rho}(\mathbf{q})$  for different QAHC- $z$  states, showing that  $|\tilde{\rho}(\mathbf{G}_i^{(z)})|$  values are on the same scale. Future experiments may identify the specific state of the system under given parameters by measuring  $\tilde{\rho}(\mathbf{q})$ . Moreover, we present the real space density profile  $\rho(\mathbf{r})$  for QAHC-1, QAHC-2, QAHC-3 in Fig. 2(a)-(c), respectively. In addition, we plot the density profile for the  $C = 1$  state at  $V_M = 5$  in Fig. 2(d). One can clearly see the different crystal periods and shapes of these phases at the same filling  $\nu = 1$ . The corresponding band structures are shown in Fig. 3.

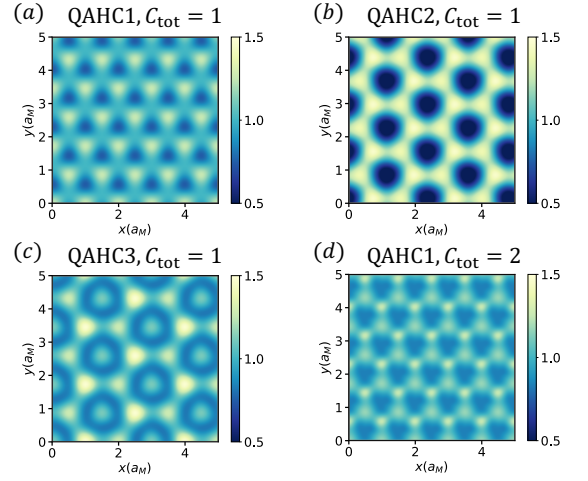


FIG. 2. In (a)-(c),  $\theta = 0.89^\circ$  ( $a_M = 10.7$  nm). The density profiles are shown for (a) ( $\delta_D = 120$  meV, QAHC-1), (b) ( $\delta_D = 160$  meV, QAHC-2) and (c) ( $\delta_D = 210$  meV, QAHC-3). In (d), we manually set  $V_M = 5$  and plot the density distribution for  $\theta = 0.78^\circ$  ( $a_M = 11.3$  nm),  $\delta_D = 190$  meV.

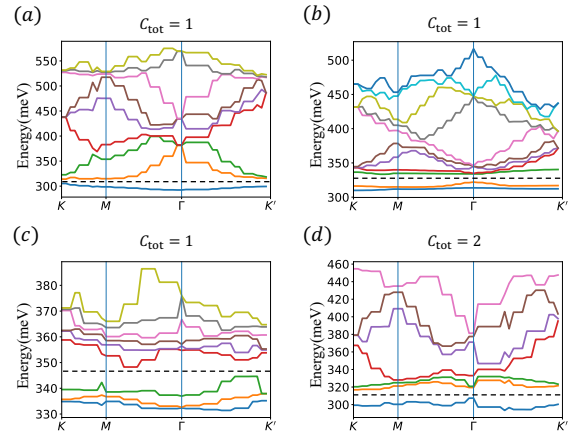


FIG. 3. The parameters used in (a)-(d) is the same as in Fig. 2 (a)-(d). The black dashed line represents the Fermi energy.

**Effect of the kinetic energy** The emergence of enlarged unit cell at  $\nu = 1$  is a surprise. Here we provide some intuition. The preference for QAHC- $z$  with  $z > 1$  arises from the kinetic energy. The band dispersion exhibits a Mexican-hat structure in the original BZ of graphene, with the band minimum forming a ring, as illustrated in Fig. 4(a). The kinetic energy of the conduction electrons can be reduced by shifting the momentum distribution,  $n_e(\mathbf{k}) = \sum_l \langle c_l^\dagger(\mathbf{k}) c_l(\mathbf{k}) \rangle$ , at  $\mathbf{k}$  to  $\mathbf{k} + \mathbf{G}_i^{(z)}$  in QAHC- $z$ . Here  $c_l(\mathbf{k})$  represents the electron operator in the graphene BZ for layer  $l$ . In the region where QAHC-2 and QAHC-3 are favored,  $\mathbf{G}_i^{(z)}$  is located around the ring of the dispersion minimum. Therefore,  $n_e(\mathbf{k})$  at the  $\Gamma$  point of the MBZ is transferred to around the dispersion minimum, reducing the

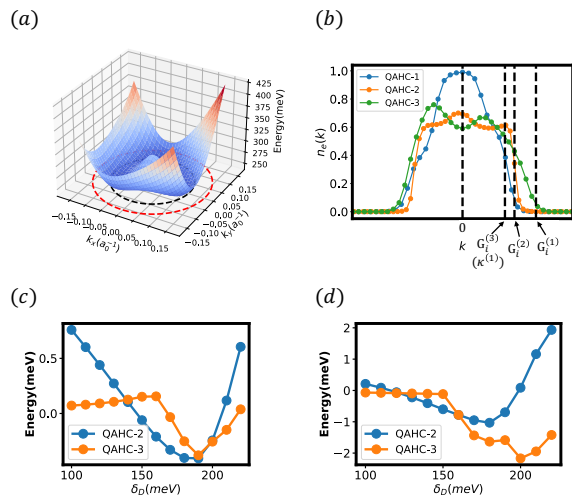


FIG. 4. The results for  $\theta = 0.89^\circ$  ( $a_M = 10.7$  nm). (a) The conduction band of pentalayer graphene in the moiréless limit at  $\delta_D = 160$  meV. The black and red dashed circle represent  $|\mathbf{k}| = |\mathbf{G}_i^{(2)}|$  and  $|\mathbf{k}| = |\mathbf{G}_i^{(1)}|$  respectively. (b) The linecut of the momentum distribution  $n_e(\mathbf{k})$  at  $\delta_D = 160$  meV. The blue, orange, green line represents QAHC-1, QAHC-2, QAHC-3 respectively. (c) The total energy and (d) the kinetic energy per moiré unit cell of QAHC- $z$  as a function of  $\delta_D$ . The blue line represents  $E_{\text{QAHC2}} - E_{\text{QAHC1}}$ , the orange line represents  $E_{\text{QAHC3}} - E_{\text{QAHC1}}$ .

total kinetic energy. As shown in Fig. 4(b), the momentum distribution  $n_e(\mathbf{k})$  at the  $\Gamma$  point is close to 1 for QAHC-1, but is considerably reduced for QAHC-2 and QAHC-3. To compare the effects of kinetic energy on total energy, we plot the line cuts of the total energy and kinetic energy of QAHC- $z$  in Fig. 4(c)(d). In the region where QAHC-2 and QAHC-3 are energetically preferred compared to QAHC-1, the kinetic energy is significantly lower for QAHC-2 and QAHC-3 compared to QAHC-1, which compensates a higher interaction energy. We conclude that the QAHC-2 and QAHC-3 phases are unique to the Mexican-hat dispersion. We expect them to be more favored for larger  $\epsilon$  with reduced interaction.

**Competition between FQAH and IQAH at  $\nu = 2/3$**  Next we turn to the fractional filling  $\nu = 2/3$ . Previous theories identify an FCI candidate through ED calculation projected onto the lowest band of the QAHC-1 insulator at  $\nu = 1$  [36–38]. However, the calculation is performed only within a subspace of the full Hilbert space and is better viewed as a variational calculation. Due to the variational nature, the method is biased towards the FCI state and ignore other candidates such as integer QAHCs with a different crystal period. The recent experiments have observed close competition between integer and fractional QAH states at fractional filling [33, 45]. To our best knowledge, there is no feasible framework to include all possible crystals in an unbiased way. Note that simply including more Hartree Fock bands from the  $\nu = 1$  QAHC-1 ansatz does not really help much, as the multi-

band calculation is still biased towards the  $a_{\text{crystal}} = a_M$  crystal and ignores the possibilities of other crystals with different periods. Here we still follow the spirit of variational calculations and compare energies of different possible ansatz.

We target the following ansatzes: (I) an FCI state at fractional filling of the lowest Chern band of the QAHC-1 crystal at  $\nu = 1$ . We obtain this state through an ED calculation. We have improved the procedure to get a self consistent crystal potential directly at the filling  $\nu = 2/3$  [37, 59] (see the Appendix). (II) We obtain various QAHC- $z$  states with integer QAH at  $\nu = 2/3$  through HF calculations. Now the crystal period is  $a_{\text{crystal}} = \sqrt{z/\nu}a_M$  and we still have  $z$  bands fully occupied.

We find the following competing states: FCI, QAHC-1 and QAHC-2. As shown in Fig. 5(a), we find that the FCI state is at slightly lower energy than the QAHC-1 state. But when increasing the dielectric constant  $\epsilon$ , the integer QAHC-1 and QAHC-2 states become more favored, though still at higher energy than the FCI within our approximation. Among the integer quantum Hall states, QAHC-2 and QAHC-1 are competing with very close energy. At small  $V_M$ , QAHC-1 has a lower energy for the ( $a_M, D$ ) parameter we used. But with a larger  $V_M$ , the energy of QAHC-2 becomes lower than that of QAHC-1, due to its commensurability with the moiré potential. We note that QAHC-2 is in the same symmetry class as a hole crystal, which can be understood as a trivial charge density wave of holes doped into the QAHC-1 state at  $\nu = 1$ . However, as we discussed in the previous section on  $\nu = 1$ , the QAHC-2 phase we find does not really rely on a parent QAH phase at a larger doping. Instead it may be viewed as a new type of quantum anomalous Hall crystal, which is favored by the moiré potential at  $\nu = 2/3$ .

In summary, we find close competition between FCI and QAHC-1 and QAHC-2 at  $\nu = 2/3$ . Within our approximations, FCI appears to always have lower energy than the integer QAH states. However, the comparison may not be fair as the QAHC-1 and QAHC-2 ansatz are obtained from Hartree Fock calculations. The only confident statement we can make is that the energies of these three states are close. Given the large tunability of the system, all of them might be realized in different parameter regions. We note that the recent experiments [33, 45] observed an integer QAH insulator at  $\nu = 2/3$ . Based on our calculation, we propose either QAHC-1 or QAHC-2 as a possible candidate, which can be only distinguished by imaging the density profile.

**Summary** In conclusion, we propose a new class of quantum anomalous Hall crystals (QAHCs) with larger crystal periods than the familiar Wigner crystal. Through Hartree Fock calculations, we demonstrate the possibility of QAHCs with doubled or tripled unit cell even at integer filling  $\nu = 1$  in pentalayer graphene aligned with hBN. We also show that the FCI state and two QAHCs are in close competitions at the fractional filling  $\nu = 2/3$ , suggesting a rich phase diagram. In our

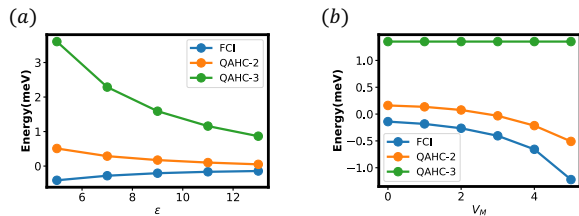


FIG. 5. HF and ED calculation at  $\delta_D = 130$  meV,  $\theta = 0.89^\circ$  ( $a_M = 10.7$  nm). (a) The energy per moiré unit cell of FCI, QAHC-2 and QAHC-3 at  $\nu = 2/3$  as a function of dielectric constant  $\epsilon$ . The blue line represents  $E_{\text{FCI}} - E_{\text{QAHC1}}$ , the orange line represents  $E_{\text{QAHC2}} - E_{\text{QAHC1}}$ , the green line represents  $E_{\text{QAHC3}} - E_{\text{QAHC1}}$ . (b) For  $\epsilon = 10$ , dependence of the energy per moiré unit cell of FCI, QAHC-1, QAHC-2 and QAHC-3 on moiré potential factor  $V_M$  at  $\nu = 2/3$ .

study we also notice the important role of the moiré potential  $V_M$ . A larger  $V_M$  can greatly change the phase diagram and even favors  $C = 2$  Chern band at  $\nu = 1$ . We hope this observation motivates more experimental efforts in controlling and enhancing the moiré potential, for example through imprinting a superlattice potential from Coulomb interaction of another control layer [37].

**Acknowledgement** BZ and YHZ thank Dacen Waters and Matthew Yankowitz for previous collaboration on related experimental work. This work was supported by a startup fund from Johns Hopkins University and the Alfred P. Sloan Foundation through a Sloan Research Fellowship (YHZ).

- [1] H. L. Stormer, D. C. Tsui, and A. C. Gossard, *Reviews of Modern Physics* **71**, S298 (1999).
- [2] J. K. Jain, *Physical review letters* **63**, 199 (1989).
- [3] K. Sun, Z. Gu, H. Katsura, and S. D. Sarma, *Physical review letters* **106**, 236803 (2011).
- [4] D. Sheng, Z.-C. Gu, K. Sun, and L. Sheng, *Nature communications* **2**, 389 (2011).
- [5] T. Neupert, L. Santos, C. Chamon, and C. Mudry, *Physical review letters* **106**, 236804 (2011).
- [6] N. Regnault and B. A. Bernevig, *Physical Review X* **1**, 021014 (2011).
- [7] E. Tang, J.-W. Mei, and X.-G. Wen, *Physical review letters* **106**, 236802 (2011).
- [8] Y.-F. Wang, Z.-C. Gu, C.-D. Gong, and D. Sheng, *Physical review letters* **107**, 146803 (2011).
- [9] E. J. Bergholtz and Z. Liu, *International Journal of Modern Physics B* **27**, 1330017 (2013).
- [10] S. A. Parameswaran, R. Roy, and S. L. Sondhi, *Comptes Rendus Physique* **14**, 816 (2013).
- [11] T. Neupert, L. Santos, S. Ryu, C. Chamon, and C. Mudry, *Phys. Rev. B* **84**, 165107 (2011).
- [12] Y.-H. Zhang, D. Mao, Y. Cao, P. Jarillo-Herrero, and T. Senthil, *Physical Review B* **99**, 075127 (2019).
- [13] F. Wu, T. Lovorn, E. Tutuc, I. Martin, and A. MacDonald, *Physical review letters* **122**, 086402 (2019).
- [14] P. J. Ledwith, G. Tarnopolsky, E. Khalaf, and A. Vishwanath, *Physical Review Research* **2**, 023237 (2020).
- [15] C. Repellin and T. Senthil, *Physical Review Research* **2**, 023238 (2020).
- [16] A. Abouelkomsan, Z. Liu, and E. J. Bergholtz, *Physical review letters* **124**, 106803 (2020).
- [17] P. Wilhelm, T. C. Lang, and A. M. Läuchli, *Physical Review B* **103**, 125406 (2021).
- [18] H. Li, U. Kumar, K. Sun, and S.-Z. Lin, *Physical Review Research* **3**, L032070 (2021).
- [19] V. Crépel and L. Fu, *Phys. Rev. B* **107**, L201109 (2023).
- [20] T. Devakul, P. J. Ledwith, L.-Q. Xia, A. Uri, S. C. de la Barrera, P. Jarillo-Herrero, and L. Fu, *Science Advances* **9**, eadi6063 (2023).
- [21] Q. Gao, J. Dong, P. Ledwith, D. Parker, and E. Khalaf, *Physical Review Letters* **131**, 096401 (2023).
- [22] S. A. A. Ghorashi, A. Dunbrack, A. Abouelkomsan, J. Sun, X. Du, and J. Cano, *Physical Review Letters* **130**, 196201 (2023).
- [23] A. L. Sharpe, E. J. Fox, A. W. Barnard, J. Finney, K. Watanabe, T. Taniguchi, M. Kastner, and D. Goldhaber-Gordon, *Science* **365**, 605 (2019).
- [24] M. Serlin, C. Tschirhart, H. Polshyn, Y. Zhang, J. Zhu, K. Watanabe, T. Taniguchi, L. Balents, and A. Young, *Science* **367**, 900 (2020).
- [25] G. Chen, A. L. Sharpe, E. J. Fox, Y.-H. Zhang, S. Wang, L. Jiang, B. Lyu, H. Li, K. Watanabe, T. Taniguchi, *et al.*, *Nature* **579**, 56 (2020).
- [26] T. Li, S. Jiang, B. Shen, Y. Zhang, L. Li, Z. Tao, T. Devakul, K. Watanabe, T. Taniguchi, L. Fu, *et al.*, *Nature* **600**, 641 (2021).
- [27] B. A. Foutty, C. R. Kometter, T. Devakul, A. P. Reddy, K. Watanabe, T. Taniguchi, L. Fu, and B. E. Feldman, *Science* **384**, 343 (2024), <https://www.science.org/doi/pdf/10.1126/science.adi4728>.
- [28] J. Cai, E. Anderson, C. Wang, X. Zhang, X. Liu, W. Holtzmann, Y. Zhang, F. Fan, T. Taniguchi, K. Watanabe, Y. Ran, T. Cao, L. Fu, D. Xiao, W. Yao, and X. Xu, *Nature* (2023), [10.1038/s41586-023-06289-w](https://doi.org/10.1038/s41586-023-06289-w).
- [29] Y. Zeng, Z. Xia, K. Kang, J. Zhu, P. Knüppel, C. Vaswani, K. Watanabe, T. Taniguchi, K. F. Mak, and J. Shan, *Nature* **622**, 69 (2023).
- [30] H. Park, J. Cai, E. Anderson, Y. Zhang, J. Zhu, X. Liu, C. Wang, W. Holtzmann, C. Hu, Z. Liu, T. Taniguchi, K. Watanabe, J.-h. Chu, T. Cao, L. Fu, W. Yao, C.-Z. Chang, D. Cobden, D. Xiao, and X. Xu, *Nature* (2023), [10.1038/s41586-023-06536-0](https://doi.org/10.1038/s41586-023-06536-0).
- [31] F. Xu, Z. Sun, T. Jia, C. Liu, C. Xu, C. Li, Y. Gu, K. Watanabe, T. Taniguchi, B. Tong, J. Jia, Z. Shi, S. Jiang, Y. Zhang, X. Liu, and T. Li, *Phys. Rev. X* **13**, 031037 (2023).
- [32] Z. Lu, T. Han, Y. Yao, A. P. Reddy, J. Yang, J. Seo, K. Watanabe, T. Taniguchi, L. Fu, and L. Ju, *arXiv preprint arXiv:2309.17436* (2023).
- [33] D. Waters, A. Okounkova, R. Su, B. Zhou, J. Yao, K. Watanabe, T. Taniguchi, X. Xu, Y.-H. Zhang, J. Folk, *et al.*, *arXiv preprint arXiv:2408.10133* (2024).
- [34] H. Yu, M. Chen, and W. Yao, *National Science Review* **7**, 12 (2020).

- [35] T. Devakul, V. Crépel, Y. Zhang, and L. Fu, *Nature communications* **12**, 6730 (2021).
- [36] Z. Dong, A. S. Patri, and T. Senthil, “Theory of fractional quantum anomalous hall phases in pentagonal rhombohedral graphene moiré structures,” (2023), [arXiv:2311.03445 \[cond-mat.str-el\]](https://arxiv.org/abs/2311.03445).
- [37] B. Zhou, H. Yang, and Y.-H. Zhang, *arXiv preprint arXiv:2311.04217* (2023).
- [38] J. Dong, T. Wang, T. Wang, T. Soejima, M. P. Zaletel, A. Vishwanath, and D. E. Parker, “Anomalous hall crystals in rhombohedral multilayer graphene i: Interaction-driven chern bands and fractional quantum hall states at zero magnetic field,” (2023), [arXiv:2311.05568 \[cond-mat.str-el\]](https://arxiv.org/abs/2311.05568).
- [39] J. Herzog-Arbeitman, Y. Wang, J. Liu, P. M. Tam, Z. Qi, Y. Jia, D. K. Efetov, O. Vafek, N. Regnault, H. Weng, *et al.*, *Physical Review B* **109**, 205122 (2024).
- [40] Z. Guo, X. Lu, B. Xie, and J. Liu, *Phys. Rev. B* **110**, 075109 (2024).
- [41] Y. H. Kwan, J. Yu, J. Herzog-Arbeitman, D. K. Efetov, N. Regnault, and B. A. Bernevig, *arXiv preprint arXiv:2312.11617* (2023).
- [42] J. Yu, J. Herzog-Arbeitman, Y. H. Kwan, N. Regnault, and B. A. Bernevig, *arXiv preprint arXiv:2407.13770* (2024).
- [43] M. Xie and S. Das Sarma, *Phys. Rev. B* **109**, L241115 (2024).
- [44] K. Huang, S. D. Sarma, and X. Li, *arXiv preprint arXiv:2408.05139* (2024).
- [45] Z. Lu, T. Han, Y. Yao, J. Yang, J. Seo, L. Shi, S. Ye, K. Watanabe, T. Taniguchi, and L. Ju, *arXiv preprint arXiv:2408.10203* (2024).
- [46] Y. Choi, Y. Choi, M. Valentini, C. L. Patterson, L. F. Holleis, O. I. Sheekey, H. Stoyanov, X. Cheng, T. Taniguchi, K. Watanabe, *et al.*, *arXiv preprint arXiv:2408.12584* (2024).
- [47] J. Xie, Z. Huo, X. Lu, Z. Feng, Z. Zhang, W. Wang, Q. Yang, K. Watanabe, T. Taniguchi, K. Liu, *et al.*, *arXiv preprint arXiv:2405.16944* (2024).
- [48] J. Ding, H. Xiang, J. Hua, W. Zhou, N. Liu, L. Zhang, N. Xin, K. Watanabe, T. Taniguchi, W. Zhu, *et al.*, *arXiv preprint arXiv:2406.14289* (2024).
- [49] Y. Zeng, D. Guerci, V. Crépel, A. J. Millis, and J. Cano, *Phys. Rev. Lett.* **132**, 236601 (2024).
- [50] T. Soejima, J. Dong, T. Wang, T. Wang, M. P. Zaletel, A. Vishwanath, and D. E. Parker, *arXiv preprint arXiv:2403.05522* (2024).
- [51] Z. Dong, A. S. Patri, and T. Senthil, *arXiv preprint arXiv:2403.07873* (2024).
- [52] T. Tan and T. Devakul, *arXiv preprint arXiv:2403.04196* (2024).
- [53] A. S. Patri, Z. Dong, and T. Senthil, *arXiv preprint arXiv:2408.11818* (2024).
- [54] S. Das Sarma and M. Xie, *Phys. Rev. B* **110**, 155148 (2024).
- [55] Z. Dong, A. S. Patri, T. Senthil, B. Zhou, H. Yang, Y.-H. Zhang, Z. M. Field, J. Dong, T. Wang, T. Wang, *et al.*, *arXiv preprint arXiv:2311.03445* (2023).
- [56] R. Su, D. Waters, B. Zhou, K. Watanabe, T. Taniguchi, Y.-H. Zhang, M. Yankowitz, and J. Folk, *arXiv preprint arXiv:2406.17766* (2024).
- [57] Y. Park, Y. Kim, B. L. Chittari, and J. Jung, *Phys. Rev. B* **108**, 155406 (2023).
- [58] C. Repellin, Z. Dong, Y.-H. Zhang, and T. Senthil, *Physical Review Letters* **124**, 187601 (2020).
- [59] K. Huang, X. Li, S. Das Sarma, and F. Zhang, *Phys. Rev. B* **110**, 115146 (2024).

## Appendix A: Projection of moiré potential

To compare the energy with different  $V_M$ , we need a consistent energy background. In the charge neutrality scheme, the vacuum is defined by fully occupying all valence bands of the bare Hamiltonian  $H_K = H_0 + V_M H_M$ . However, the vacuum energy varies with different  $V_M$ . There are two ways to address this: (1) Moiréless charge neutrality scheme: This approach defines the vacuum by occupying all valence bands in the moiréless limit, as described in Ref. [59]. However, the leading order contribution from the moiré potential diverges, as shown in Fig. 2(b) of Ref. [59]. Therefore, we consider the second way, which is using moiré charge neutrality scheme with projection: We still use the moiré charge neutrality scheme, but project the moiré potential onto the conduction bands. This ensures that the vacuum energy remains consistent for different  $V_M$ .

The original moiré potential is given by:

$$H_M = \sum_{\mathbf{k}} \sum_{j=1}^6 \psi_1^\dagger(\mathbf{k}) H_M(\mathbf{G}_j) \psi_1(\mathbf{k} + \mathbf{G}_j), \quad (\text{A1})$$

where  $H_M(\mathbf{G}_j)$  is defined in Eq. (6) of the main text, and  $\psi_z(\mathbf{k}) = (f_{z,A}(\mathbf{k}), f_{z,B}(\mathbf{k}))^T$  represents the spin-valley polarized electron operator for the two sublattice in layer  $z$ . There is only  $\psi_1(\mathbf{k})$  in  $H_M$  because the moiré potential only acts on the first layer aligned with the hBN.

To obtain the projection operator, we diagonalize the moiréless pentagonal graphene Hamiltonian  $H_0$ , defined in Eq. (2) of the main text for each  $\mathbf{k}$ . This yields the matrix form of the projection operator for conduction electrons

at each  $\mathbf{k}$ , denoted as  $P_c(\mathbf{k})$ . The projected moiré potential is then:

$$\tilde{H}_M = \sum_{\mathbf{k}} \sum_{j=1}^6 \psi_1^\dagger(\mathbf{k}) P_c(\mathbf{k}) H_M(\mathbf{G}_j) P_c(\mathbf{k} + \mathbf{G}_j) \psi_1(\mathbf{k} + \mathbf{G}_j). \quad (\text{A2})$$

### Appendix B: Hartree Fock calculation

We perform Hartree Fock calculation by keeping the first  $N_{b,c}$  conduction bands and the first  $N_{b,v}$  valence bands in the MBZ. The interaction term can be written as:

$$H_V = \frac{1}{2A} \sum_{\mathbf{q}} \sum_{l,l'} V_{l,l'}(\mathbf{q}) : \rho_l(\mathbf{q}) \rho_{l'}(-\mathbf{q}) :, \quad (\text{B1})$$

where  $\rho_l(\mathbf{q}) = \sum_{\mathbf{k}, m, m'} c_m^\dagger(\mathbf{k} + \mathbf{q}) \Lambda_{m,m'}^l(\mathbf{k}, \mathbf{q}) c_{m'}(\mathbf{k})$  represents the density at layer  $l$ . Here  $\Lambda_{m,m'}^l(\mathbf{k}, \mathbf{q}) = \langle u_m(\mathbf{k} + \mathbf{q}) | P_l | u_{m'}(\mathbf{k}) \rangle$ ,  $P_l$  is the projection operator to layer  $l$ ,  $m$  and  $m'$  are band indices. For  $m = 0, 1, \dots, N_{b,v} - 1$ , the indices correspond to the valence bands. For  $m = N_{b,v}, N_{b,v} + 1, \dots, N_{b,v} + N_{b,c} - 1$ , the indices correspond to the conduction bands. The interaction is given by:

$$V_{l,l'}(\mathbf{q}) = \frac{e^2 e^{-q|l-l'|d_{\text{layer}}} \tanh(|\mathbf{q}|\lambda)}{2\epsilon\epsilon_0|\mathbf{q}|}, \quad (\text{B2})$$

where  $d_{\text{layer}}$  is the distance between adjacent layers,  $\lambda$  is the screening length. We choose  $d_{\text{layer}} = 0.34$  nm and  $\lambda = 30$  nm in our calculation. The interaction can be decoupled into Hartree and Fock terms, leading to a mean field Hamiltonian:

$$H_{\text{HF}} = \sum_{\mathbf{k}_1, \mathbf{k}_2} \sum_{m, m', n, n'} 2 (V_{m, m', n, n'}(\mathbf{k}_1, \mathbf{k}_2, \mathbf{0}) - V_{n, m', m, n'}(\mathbf{k}_1, \mathbf{k}_2, \mathbf{k}_2 - \mathbf{k}_1)) \quad (\text{B3})$$

$$(\langle c_m^\dagger(\mathbf{k}_1) c_{m'}(\mathbf{k}_1) \rangle - \delta_{m, m', \text{valence}}) c_n^\dagger(\mathbf{k}_2) c_{n'}(\mathbf{k}_2), \quad (\text{B4})$$

where  $m, m', n, n'$  are band indices.  $\delta_{m, m', \text{valence}} = 1$  while  $m = m'$  and  $m$  is valence band, otherwise it is 0. We include this term because we use the charge neutrality scheme, in which the reference state is all of the valence bands are occupied. The expectation value  $\langle c_m^\dagger(\mathbf{k}_1) c_{m'}(\mathbf{k}_1) \rangle$  is calculated by using the free fermion mean field state given by  $H_K + H_{\text{HF}}$ , with all valence bands and  $z$  conduction bands occupied. Here  $z$  corresponds to the QAHC- $z$  ansatz. The interaction vertex is calculated as:

$$V_{m, m', n, n'}(\mathbf{k}_1, \mathbf{k}_2, \mathbf{q}) = \frac{1}{2A} \sum_{l, l'} V_{l, l'}(\mathbf{q}) \Lambda_{m, m'}^l(\mathbf{k}_1, \mathbf{q}) \Lambda_{n, n'}^{l'}(\mathbf{k}_2, -\mathbf{q}). \quad (\text{B5})$$

The mean field energy is calculated as:

$$E_{\text{MF}} = \sum_{\mathbf{k}, n} \epsilon_n(\mathbf{k}) (\langle c_n^\dagger(\mathbf{k}) c_n(\mathbf{k}) \rangle - \delta_{n, \text{valence}}) \quad (\text{B6})$$

$$+ \sum_{\mathbf{k}_1, \mathbf{k}_2} \sum_{m, m', n, n'} (V_{m, m', n, n'}(\mathbf{k}_1, \mathbf{k}_2, \mathbf{0}) - V_{n, m', m, n'}(\mathbf{k}_1, \mathbf{k}_2, \mathbf{k}_2 - \mathbf{k}_1)) \quad (\text{B7})$$

$$(\langle c_m^\dagger(\mathbf{k}_1) c_{m'}(\mathbf{k}_1) \rangle - \delta_{m, m', \text{valence}}) (\langle c_n^\dagger(\mathbf{k}_2) c_{n'}(\mathbf{k}_2) \rangle - \delta_{n, n', \text{valence}}), \quad (\text{B8})$$

in which  $\delta_{n, \text{valence}} = 1$  while  $n$  is valence band, otherwise it is 0.  $\epsilon_n(\mathbf{k})$  is the dispersion of the  $n^{\text{th}}$  band of  $H_K$ . In our HF calculation, we try 40 number of randomized initial ansatz and choose the one with the lowest energy.

### Appendix C: ED calculation

We perform ED calculation by projecting the Coulomb interaction into the lowest conduction HF band, which is the  $(N_{b,v} + 1)^{\text{th}}$  lowest HF band. The total Hamiltonian is expressed as:

$$H = \sum_{\mathbf{k}} \epsilon(\mathbf{k}) \tilde{c}_{N_{b,v}}^\dagger(\mathbf{k}) \tilde{c}_{N_{b,v}}(\mathbf{k}) + \sum_{\mathbf{k}_1, \mathbf{k}_2, \mathbf{q}} V(\mathbf{k}_1, \mathbf{k}_2, \mathbf{q}) \tilde{c}_{N_{b,v}}^\dagger(\mathbf{k}_1 + \mathbf{q}) \tilde{c}_{N_{b,v}}^\dagger(\mathbf{k}_2 - \mathbf{q}) \tilde{c}_{N_{b,v}}(\mathbf{k}_2) \tilde{c}_{N_{b,v}}(\mathbf{k}_1), \quad (\text{C1})$$

where  $\tilde{c}_{N_b,v}^\dagger(\mathbf{k}) = \sum_n U_{N_b,vn}(\mathbf{k})c_n^\dagger(\mathbf{k})$  represents the electron operator of the lowest conduction HF band, with  $c_n^\dagger(\mathbf{k})$  being the electron operator in bare Hamiltonian  $H_K$ , and  $n$  indexing the bands. The dispersion  $\epsilon(\mathbf{k})$  is obtained by projecting the dispersion of the kinetic term  $H_K = H_0 + V_M H_M$  onto the lowest conduction HF band:

$$\epsilon(\mathbf{k}) = \sum_n |U_{N_b,vn}(\mathbf{k})|^2 \epsilon_n(\mathbf{k}), \quad (\text{C2})$$

where  $\epsilon_n(\mathbf{k})$  is the dispersion of the  $n^{\text{th}}$  band of  $H_K$ . The interaction vertex takes the form:

$$V(\mathbf{k}_1, \mathbf{k}_2, \mathbf{q}) = \frac{1}{2A} \sum_{l,l'} V_{l,l'}(\mathbf{q}) \Lambda_{\text{HF}}^l(\mathbf{k}_1, \mathbf{q}) \Lambda_{\text{HF}}^{l'}(\mathbf{k}_2, -\mathbf{q}), \quad (\text{C3})$$

where  $\Lambda_{\text{HF}}^l(\mathbf{k}_1, \mathbf{q}) = \langle u_{\text{HF},N_b,v}(\mathbf{k}_1 + \mathbf{q}) | P_l | u_{\text{HF},N_b,v}(\mathbf{k}_1) \rangle$  is the form factor of the lowest conduction HF Bloch wavefunction on layer  $l$ .

Applying the particle-hole transformation  $\tilde{c}_{N_b,v}(\mathbf{k}) \rightarrow \tilde{h}_{N_b,v}^\dagger(\mathbf{k})$ , we obtain the total Hamiltonian including the kinetic and interaction term:

$$\begin{aligned} H = & - \sum_{\mathbf{k}} \left( \epsilon(\mathbf{k}) + 2 \sum_{\mathbf{k}'} (V(\mathbf{k}, \mathbf{k}', \mathbf{0}) - V(\mathbf{k}, \mathbf{k}', \mathbf{k} - \mathbf{k})) \right) \tilde{h}_{N_b,v}^\dagger(\mathbf{k}) \tilde{h}_{N_b,v}(\mathbf{k}) \\ & + \sum_{\mathbf{k}_1, \mathbf{k}_2, \mathbf{q}} V(\mathbf{k}_1, \mathbf{k}_2, \mathbf{q}) \tilde{h}_{N_b,v}^\dagger(\mathbf{k}_1 + \mathbf{q}) \tilde{h}_{N_b,v}^\dagger(\mathbf{k}_2 - \mathbf{q}) \tilde{h}_{N_b,v}(\mathbf{k}_2) \tilde{h}_{N_b,v}(\mathbf{k}_1) + E_0. \end{aligned} \quad (\text{C4})$$

Here  $\epsilon(\mathbf{k}) - \sum_{\mathbf{k}'} (V(\mathbf{k}, \mathbf{k}', \mathbf{0}) - V(\mathbf{k}, \mathbf{k}', \mathbf{k} - \mathbf{k}))$  equals to the HF dispersion.  $E_0$  is the energy of the  $\nu = 1$  insulating state:

$$E_0 = \sum_{\mathbf{k}} \left( \epsilon(\mathbf{k}) + \sum_{\mathbf{k}'} (V(\mathbf{k}, \mathbf{k}', \mathbf{0}) - V(\mathbf{k}, \mathbf{k}', \mathbf{k} - \mathbf{k})) \right). \quad (\text{C5})$$

Therefore, we are using the hole picture relative to the  $\nu = 1$  state, applying the dispersion and the form factor of the HF band to perform the ED calculation.

In the ED calculation, we define the many body Hamiltonian in the hole picture relative to the  $\nu = 1$  spin-valley polarized Chern insulator. We stress that performing the calculation in the electron picture will lead to double-counting issues. In our main text,  $\nu = 2/3$  filling is treated as  $1/3$  filling in terms of holes relative to the  $\nu = 1$  Chern insulator. Since the  $\nu = 1$  parent state is spin-valley polarized, the hole creation operator of the other spin or valley species is meaningless, allowing us to access only spin-valley polarized FCI states within this framework.

#### Appendix D: Self consistent ED calculation at fractional filling beyond the rigid band approximation

We go beyond the rigid band approximation and perform a self consistent calculation at  $\nu = 2/3$  directly. The procedure is similar to the standard self consistent HF calculation in Eq. B4, but in this case, the expectation value  $\langle c_m^\dagger(\mathbf{k}_1) c_{m'}(\mathbf{k}_1) \rangle$  is directly obtained from the many body FCI state at  $\nu = 2/3$ , instead of a free fermion mean field state. During each iteration, we get bands from the mean field Hamiltonian  $H_K + H_{\text{HF}}$ , where the creation operator  $\tilde{c}_m^\dagger(\mathbf{k})$  corresponds to the  $m = 0, 1, \dots$  bands.

An FCI state at  $\nu = 2/3$  can be constructed for the band generated by  $\tilde{c}_{N_b,v}(\mathbf{k})$ . In principle, we can use ED to get the FCI state and calculate the expectation value, which enters the self consistent equation in Eq. B4 to generate a new  $H_{\text{MF}}$ . However, we simplify the process by noting that the FCI state has an almost uniform momentum distribution. Thus, we approximately have:

$$\langle \tilde{c}_m^\dagger(\mathbf{k}_1) \tilde{c}_{m'}(\mathbf{k}_1) \rangle \approx \nu \delta_{m,N_b,v} \delta_{m',N_b,v}, \quad (\text{D1})$$

where  $\tilde{c}_m^\dagger(\mathbf{k}) = \sum_n U_{mn}(\mathbf{k}) c_n^\dagger(\mathbf{k})$  is the electron operator of the  $m^{\text{th}}$  mean field band and  $c_n^\dagger(\mathbf{k})$  is the electron operator in the band of the bare  $H_K$ , with  $n$  is the bare band index. The expectation value  $\langle c_m^\dagger(\mathbf{k}_1) c_{m'}(\mathbf{k}_1) \rangle$  which enters Eq. B4 can now be calculated as:

$$\langle c_m^\dagger(\mathbf{k}_1) c_{m'}(\mathbf{k}_1) \rangle \approx \nu U_{N_b,vm}^*(\mathbf{k}_1) U_{N_b,vm'}(\mathbf{k}_1). \quad (\text{D2})$$



### Appendix E: Integer QAHC- $z$ at $\nu = 2/3$

Besides the FQAH states at  $\nu = 2/3$ , we also target the integer QAHC- $z$  as variational ansatzes. As discussed in the main text, for  $z/\nu = m_1^2 + m_2^2 + m_1 m_2$  with  $m_1, m_2 \in \mathbb{Z}$ , the moiré potential is commensurate with the crystal period. We consider  $z = 1, 2, 3$ , only QAHC-2 is commensurate with the moiré potential. In this case,  $a_{\text{crystal}} = \sqrt{z/\nu} a_M = \sqrt{3} a_M$ . Suppose the reciprocal vector of the QAHC-2 crystal at  $\nu = 2/3$  is  $\mathbf{g}_j$ ,  $j = 1, 2, 3, 4, 5, 6$ . The relation between  $\mathbf{G}_j$  and  $\mathbf{g}_j$  is:

$$\mathbf{G}_1 = \mathbf{g}_1 - 2\mathbf{g}_2, \quad (\text{E1})$$

$$\mathbf{G}_2 = 2\mathbf{g}_1 - \mathbf{g}_2, \quad (\text{E2})$$

$$\mathbf{G}_3 = \mathbf{g}_1 + \mathbf{g}_2, \quad (\text{E3})$$

$$\mathbf{G}_4 = -\mathbf{g}_1 + 2\mathbf{g}_2, \quad (\text{E4})$$

$$\mathbf{G}_5 = -2\mathbf{g}_1 + \mathbf{g}_2, \quad (\text{E5})$$

$$\mathbf{G}_6 = -\mathbf{g}_1 - 2\mathbf{g}_2. \quad (\text{E6})$$

Then we can write the moiré potential in the basis of  $\mathbf{g}_j$  and perform the calculations.

### Appendix F: Details of QAHC- $z$ energy

We present the energy per moiré unit cell for QAHC- $z$  with  $z = 1, 2, 3$  in Fig. 6(a), (b), (c) respectively. The blank regions correspond to the metal phase or the trivial Wigner crystal phase. The calculations were conducted with  $\epsilon = 10$ . For QAHC-1 and QAHC-2, we keep  $N_{b,v} = 0$  valence bands and  $N_{b,c} = 7$  conduction bands, using a  $12 \times 12$  grid in the crystal Brillouin zone for the HF calculations. For QAHC-3, we keep  $N_{b,v} = 0$  valence bands and  $N_{b,c} = 9$  conduction bands, using a  $9 \times 9$  grid in the crystal Brillouin zone for the HF calculations. We also show the energy difference of different QAHC states in Fig. 6(d)-(f), in which we only keep the negative value.

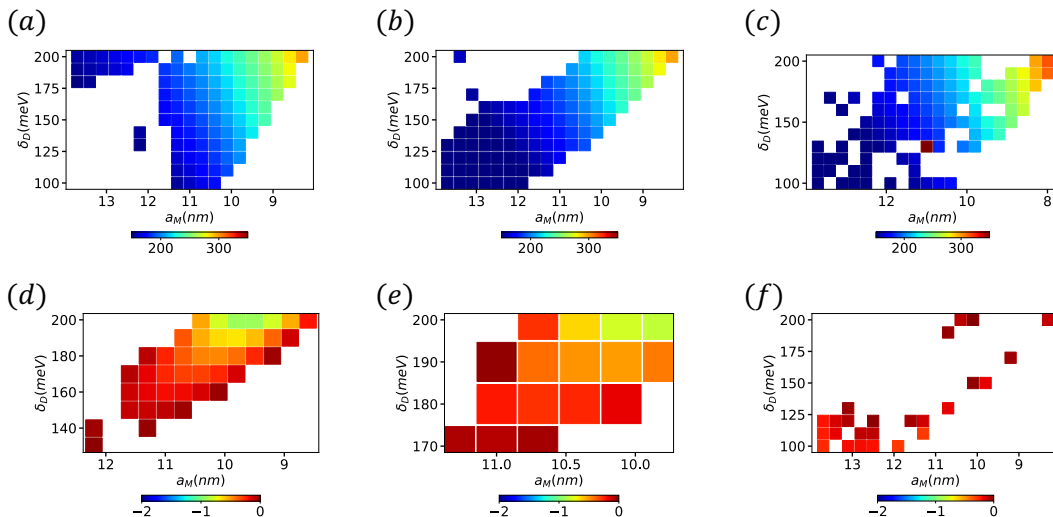


FIG. 6. The energy per moiré unit cell for (a) QAHC-1, (b) QAHC-2 and (c) QAHC-3. The energy difference per moiré unit cell for (d)  $E_{\text{QAHC2}} - E_{\text{QAHC1}}$ , (e)  $E_{\text{QAHC3}} - E_{\text{QAHC1}}$  and (f)  $E_{\text{QAHC3}} - E_{\text{QAHC2}}$ .

### Appendix G: Demonstration of convergence in HF calculation

In the main text, we set  $N_{b,v} = 0$  and  $N_{b,c} = 7, 7, 9$  for QAHC-1, QAHC-2, and QAHC-3 respectively to perform the Hartree Fock calculation. The calculations are performed using an  $N_k \times N_k$  grid in the crystal BZ, with  $N_k$  set to 12, 12, and 9 for  $z = 1, 2, 3$ , respectively. To demonstrate the convergence of our calculation, we select specific parameters with  $\delta_D = 160$  meV and  $\theta = 0.89^\circ$  ( $a_M = 10.7$  nm), and then increase  $N_{b,c}$  and  $N_k$  to perform the calculation, as shown in Fig. 7(a)(b) respectively. In the limit  $N_{b,c} \rightarrow \infty$  and  $N_k \rightarrow \infty$ , the QAHC-2 state converges to have the lowest energy.

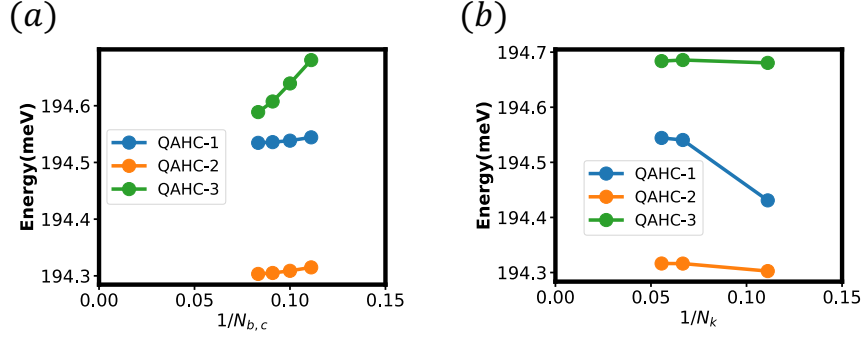


FIG. 7. (a) The energy per moiré unit cell of QAHC- $z$  varies with  $1/N_{b,c}$ . The energy difference converges to a positive value as  $N_{b,c} \rightarrow \infty$ . For  $z = 1, 2, 3$ , we choose  $N_k = 18, 12, 9$  respectively. (b) The energy per moiré unit cell for QAHC- $z$  with  $z = 1, 2, 3$  is plotted as a function of  $1/N_k$ . We choose  $N_{b,c} = 9$  for  $z = 1, 2, 3$ .

### Appendix H: Phase diagram with another parameter

In other reference [38], people use a different set of parameters. The parameters they used are  $(\gamma_0, \gamma_1, \gamma_2, \gamma_3, \gamma_4) = (-3100, 380, -21, 290, 141)$  meV. Compared to Eq. 3 in the main text, they assume the potential difference is uniform in the system and ignore the term of  $u_{A,i}$ ,  $u_{B,i}$ . For the moiré potential term, it is:

$$H_M(\mathbf{G}_j) = \begin{pmatrix} V_0 + V_1 e^{i\psi} & V_1 e^{i(\frac{3-j}{3}\pi + \psi)} \\ V_1 e^{i(\frac{1+j}{3}\pi + \psi)} & V_0 + V_1 e^{i(-\frac{2}{3}\pi + \psi)} \end{pmatrix}, \quad (\text{H1})$$

where the momentum difference given by  $\mathbf{G}_j = \frac{4\pi}{\sqrt{3}L_M} (\cos(\frac{j\pi}{3} - \frac{5\pi}{6}), \sin(\frac{j\pi}{3} - \frac{5\pi}{6}))^T$  for  $j = 1, 3, 5$ . For  $j = 2, 4, 6$ , the tunneling is obtained by taking the Hermitian conjugate. The parameters are  $(V_0, V_1, \psi) = (28.9 \text{ meV}, 21 \text{ meV}, -0.29)$ .

We use the new parameter for the free Hamiltonian  $H_K$  and retain the same parameters as in the main text,  $(\lambda, d_{\text{layer}}, \epsilon) = (30 \text{ nm}, 0.34 \text{ nm}, 10)$ , for the Coulomb interaction term  $H_V$  to perform the Hartree Fock calculation, obtaining the phase diagram at  $\nu = 1$  shown in Fig. 8.

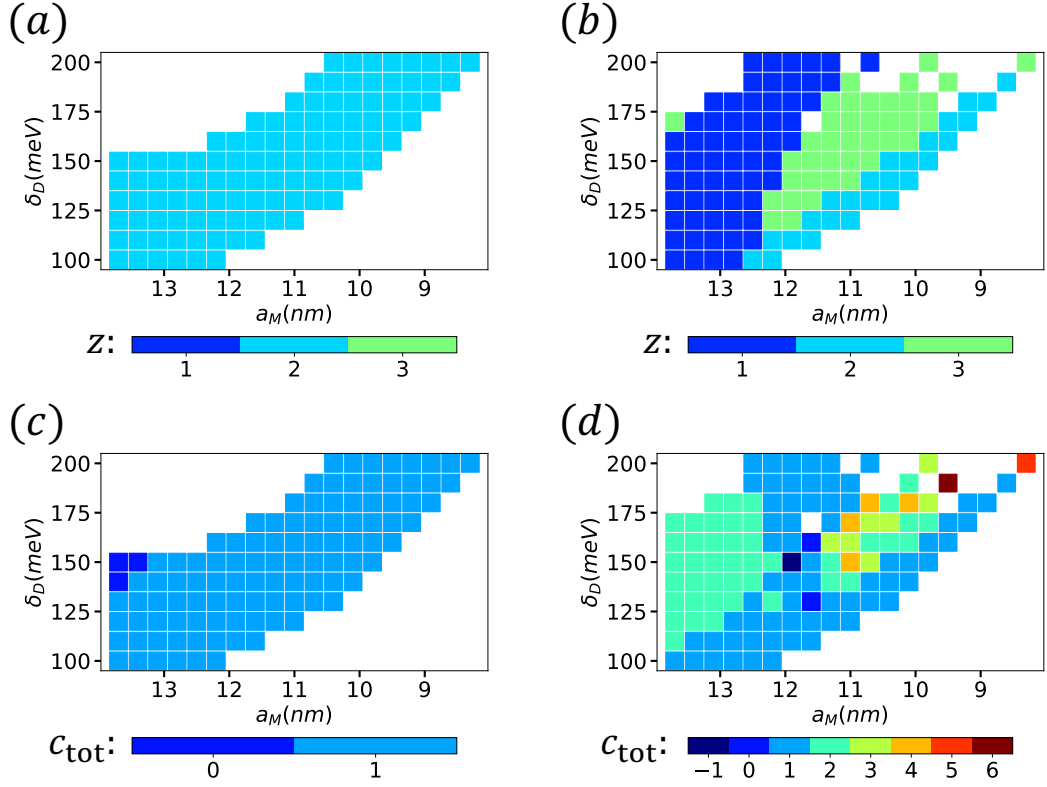


FIG. 8. (a) The phase diagram of QAHC as a function of displacement field  $D$  and moiré period  $a_M$ . We keep  $N_{b,c}$  conduction bands and  $N_{b,v}$  valence bands in the calculation. For QAHC- $z$  with  $z = 1, 2, 3$ , we set  $N_{b,c}$  to 7, 7 and 9 respectively.  $N_{b,v}$  is taken as 0 for all values of  $z$ , since the valence bands are separated by the large displacement field. The calculations are performed using an  $N_k \times N_k$  grid in the crystal BZ. For  $z = 1, 2, 3$ , we set  $N_k$  to 12, 12 and 9 respectively. (a) Dependence of  $z$  on  $D$  and  $a_M$  for  $V_M = 1$ . (b) Dependence of  $z$  on  $D$  and  $a_M$  for  $V_M = 2$ . (c) Dependence of  $C_{\text{tot}}$  on  $D$  and  $a_M$  for  $V_M = 1$ . (d) Dependence of  $C_{\text{tot}}$  on  $D$  and  $a_M$  for  $V_M = 2$ .